nature communications

Article

https://doi.org/10.1038/s41467-025-60489-8

Substrate-based discovery of α-hydroxycarboxylic acid derivatives as potential herbicides targeting dihydroxyacid dehydratase

Received: 19 February 2025

Accepted: 23 May 2025

Published online: 04 June 2025

Check for updates

Bo He[1,5], Yanhao Hu[1,5], Dongshan Liu[2,5], Xin Zang[2], Xu He[1], Wang Chen[1], Jingfang Yang[3], Mingfeng Feng[1], Ping Chen[1], Lirong Wei[1], Yu Li[1], Wei Yan[1], Jun Li[1], Zhike Feng[1], Jiahai Zhou[2,4] ✉ & Yonghao Ye[1] ✉

Dihydroxyacid dehydratase (DHAD), a key enzyme in branched-chain amino acid synthesis in plants, is a promising yet unexploited herbicide target. Inspired by the natural DHAD inhibitor aspterric acid, we design benzoxazinone derivatives with α-hydroxycarboxylic acid moieties as potential inhibitors and develop an eco-friendly α-C(sp^3)-H hydroxylation method for accessing carbonyl compounds. Among the derivatives, 7-fluoro-2-hydroxy-3-oxo-4-propyne-3,4-dihydro-2*H*-benzo[*b*][1,4]oxazine-2-carboxylic acid (**I-6e**) completely inhibits *Arabidopsis thaliana* germination and suppress six weed species by > 50%, with 100% efficacy against *Avena fatua* and *Setaria viridis* at 150 g ai/ha. This broad-spectrum activity and rice crop safety highlight its potential as an herbicide lead compound. Compound **I-6e** exhibits stronger affinity for DHAD (K_d = 1 μM) than that of the natural substrate (K_d = 5.39 μM). The 2.19 Å cocrystal structure of the *At*DHAD–**I-6e** complex reveals a unique binding mechanism, confirming the critical role of the α-hydroxycarboxylic acid scaffold. This study provides a blueprint for rational DHAD inhibitor design.

Herbicides have been a mainstay in agriculture to protect crops against weed infestations for more than 70 years. Currently, agricultural practices require agrochemicals to be highly efficient and selective and environmentally and ecologically safe[1]. Branched-chain amino acids (BCAAs; valine, leucine, and isoleucine) are fundamental building blocks of proteins that are synthesized in bacteria, plants, and fungi but not in animals. Therefore, inhibitors targeting the BCAA synthesis pathway exhibit high selectivity among animals, plants and microorganisms. Therefore, enzymes integral to the BCAA biosynthetic pathway are considered prime targets for the development of selective herbicides[2–4]. The initial steps in the BCAA biosynthetic pathway involve acetolactate synthase (AHAS)[5], acetohydroxy acid isomeroreductase (KARI)[6], and dihydroxyacid dehydratase (DHAD) (Fig. 1a)[7]. To date, more than 50 herbicides targeting AHAS have been developed and widely used[8]. While these classes of herbicides have high efficacy and established safety

[1]State Key Laboratory of Agricultural and Forestry Biosecurity, State & Local Joint Engineering Research Center of Green Pesticide Invention and Application, College of Plant Protection, Nanjing Agricultural University, Nanjing 210095, China. [2]State Key Laboratory of Chemical Biology, Center for Excellence in Molecular Synthesis, Shanghai Institute of Organic Chemistry, Chinese Academy of Science, Shanghai 200032, China. [3]State Key Laboratory for Biology of Plant Diseases and Insect Pests, Institute of Plant Protection, Chinese Academy of Agricultural Sciences, Beijing 100193, China. [4]School of Food Science and Pharmaceutical Engineering, Nanjing Normal University, Nanjing 210023, China. [5]These authors contributed equally: Bo He, Yanhao Hu, Dongshan Liu. ✉e-mail: jiahai@nnu.edu.cn; yeyh@njau.edu.cn

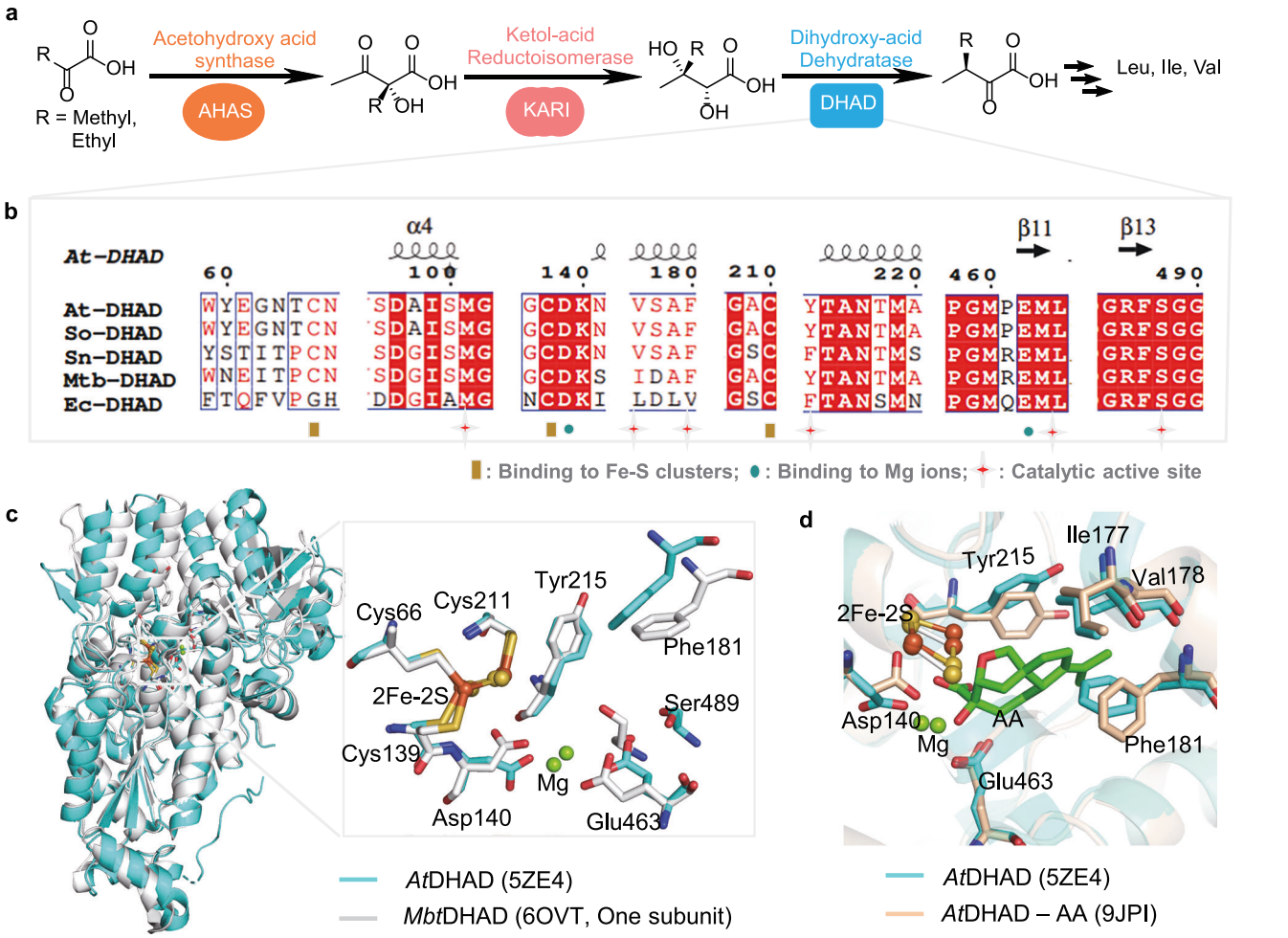

Fig. 1 | Structure and function of DHAD and its catalytic mechanism. **a** Branched-chain amino acid biosynthetic pathway. **b** Amino acid sequence alignment of DHADs from *Arabidopsis thaliana* (*At*DHAD, 5ZE4), *Spinacia oleracea* (*So*DHAD, XP_021849033.1), *Synechocystis* sp. *PCC 6803* (*Sn*DHAD, 6NTE), *Mycobacterium tuberculosis* (*Mtb*DHAD, 6OVT) and *Escherichia coli* (*Ec*DHAD, ACX41805.1). The truncated sequences primarily display key amino acid residues within the catalytic active site of the protein. **c** Superposition of the three-dimensional structures of *At*DHAD and *Mtb*DHAD and residues in the active pocket. **d** Superposition of the three-dimensional structures of *At*DHAD–AA (9JPI) and *At*DHAD (5ZE4). Conformational changes in amino acid residues in the active pocket.

profiles, the emergence of weed resistance presents a significant problem for their long-term usage. Not only are AHAS-inhibiting herbicides encountering the development of resistance, but most other herbicides with alternative targets have also succumb to resistance issues. This underscores the urgent need to discover active herbicides with alternative modes of action.

DHAD, a member of the IlvD/EDD protein family, is encoded by a single gene in plants[9]. In contrast to the well-researched enzyme AHAS, DHAD has not been as extensively explored as a target for the development of herbicides. Dennis H. Flint pioneered the synthesis of a series of derivatives that aimed to inhibit DHAD with inhibition constants (K_i values) in the submicromolar range[10]. However, despite their effectiveness as DHAD inhibitors, these compounds do not exhibit herbicidal activity[10]. Leveraging a resistance gene-directed approach, the natural product aspterric acid (**AA**) was found to target DHAD and exhibits herbicidal activity against glufosinate-resistant *Arabidopsis thaliana* at a concentration of 250 μM[2]. Subsequently, the Zhou group reported the crystal structure of **AA** with *A. thaliana* DHAD (*At*DHAD), which shows that hydroxycarboxylic acid moiety binds with Mg^{2+} and that hydrogen bonding networks and hydrophobic interactions stabilize **AA** in the enzyme active site[11]. The well-understood interactions between DHAD and this inhibitor represent a significant breakthrough in the rational design of DHAD inhibitors. Recently, DHAD has gained attention not only as a target for herbicidal action but also as a promising candidate for the precise growth control of microbes[2,3,7]. In 2019, the Ding group reported that tartronic acid (**TA**) inhibited the growth of cyanobacteria by targeting DHAD[3]. Despite our comprehensive understanding of the structure and function of DHAD, designing inhibitor molecules for this novel target remains a significant challenge. However, innovative approaches, including structure-based iterative learning[12], peptidomimetics[13,14], and virtual synthon hierarchical enumeration screening (V-SYNTHES)[15,16], offer promising pathways forward. Nevertheless, when the mechanism of action of an inhibitor on its target is not completely understood, the reliability of applying existing data models to swiftly and precisely identify target inhibitors remains uncertain.

In this study, leveraging a model of substrates bound to DHAD, we adopt a substrate-based strategy to design a series of benzoxazinone derivatives incorporating an α-hydroxycarboxylic acid fragment and develop an efficient method to synthesize target compounds. Microscale thermophoresis (MST) assays reveal that compounds **I-6c**, **I-6e**, **I-6g**, **I-6j**, and **I-6i** have stronger binding affinities for DHAD than the natural substrate does. In addition, the cocrystal structure of *At*DHAD in complex with **I-6e** is determined at 2.19 Å resolution, revealing how the inhibitor interacts within the active site pocket. These results are

instrumental in guiding the future design of targeted DHAD inhibitors with significant potential for agricultural use.

Results

Structure of DHAD and its active site

All DHADs from different species contain [2Fe-2S] or [4Fe-4S] clusters, which are essential for the catalytic function of these enzymes[17]. The [4Fe-4S] cluster was initially observed in DHAD from *Escherichia coli*, while the [2Fe-2S] cluster was first reported in DHAD from *spinach*[17,18]. Although the [2Fe-2S] cluster is more stable in the presence of oxygen than the [4Fe-4S] cluster, both DHADs can be inactivated under aerobic conditions[3,7]. The oxygen sensitivity of DHAD proteins does indeed present a challenge for experimental studies, particularly when aiming to elucidate their catalytic mechanism and interactions with inhibitors.

Recently, crystal structures of DHADs from *A. thaliana*[2], *Mycobacterium tuberculosis*[19], and *Synechocystis* sp. PCC 6803[3] have been obtained, which provide insights into how DHAD substrates interact with this enzyme. Amino acid sequence alignment of revealed that the sequence similarity between *A. thaliana* and *spinach* DHADs exceeded 83% (Supplementary Table 1), whereas greater sequence divergence was observed between plant DHADs and those from fungi and bacteria (Supplementary Fig. 1). Despite structural variations in holo-DHADs across species, the key amino acid residues that interact with iron–sulfur clusters and Mg^{2+} ions remain highly conserved (Fig. 1b)[2,3,19]. Comparative analysis of a single subunit from the crystal structures of *At*DHAD (PDB ID: 5ZE4) and *M. tuberculosis* DHAD (*Mtb*DHAD, PDB ID: 6OVT) (Fig. 1c) revealed that the configurations of the three cysteine residues coordinating with the 2Fe-2S cluster were essentially identical. However, a notable shift was observed in the positions of the Asp140 and Glu463 residues associated with the binding of Mg^{2+}. Additionally, the spatial arrangements of several key residues within the active site involved in substrate interactions (Phe181, Ser489, and Tyr215) were altered. These differences can be exploited to develop species-specific inhibitors that selectively target the DHAD enzyme in one organism without affecting the same enzyme in another, which is particularly valuable in the development of selective herbicides. The cocrystal structure of *At*DHAD–**AA** has been reported (PDB ID: 9JPI)[11]. When **AA** binds to the active site of *At*DHAD, Tyr215, Phe181 and Asp140 exhibit significant conformational changes, as shown in the superimposed crystal structure (Fig. 1d). Furthermore, the mutations I177F and V178F in *At*DHAD have been shown to decrease the stability of **AA** binding to DHAD. On the other hand, during the enzymatic reaction catalyzed by DHAD, the coordination interactions between the substrate and the metal ions (iron–sulfur clusters and Mg^{2+}) and the hydrogen bonding interactions with neighboring amino acids are crucial[10,19]. These interactions provide a theoretical foundation for designing the molecular framework of targeted DHAD inhibitors.

Substrate-based molecular design

In the model of *At*DHAD bound with its natural substrate, 2,3-dihydroxy-3-methylbutanoic acid (Fig. 2a), the α-hydroxycarboxylic acid moiety not only coordinates with the iron–sulfur clusters but also engages with Mg^{2+} and forms hydrogen bonds with Glu463. These findings suggest that the α-hydroxycarboxylic acid fragment is a critical component and should be included in the design of improved DHAD inhibitors. In addition to coordination interactions, the aromatic amino acid residues Tyr215 and Phe181 establish hydrophobic contacts with the substrate. This observation indicates that hydrophobic interactions are another fundamental aspect of the inhibitor structure. These key binding residues are also observed in the crystal structure of the *At*DHAD–**AA** complex. These findings imply that incorporating aromatic groups into the inhibitor skeleton may allow the formation of π–π interactions with neighboring residues Tyr215 or Phe181, as well as hydrophobic interactions with Ile177. Additionally, Ser489 interacts with the substrate via hydrogen bonds, which increases the stability of a small molecule in the active cavity and the binding affinity of an inhibitor to the enzyme.

Additionally, a benzoxazinone skeleton from the pesticide fragment bank attracted our attention because of its extensive biological activity in the pharmaceutical and agrochemical fields[20,21]. This core structure is particularly prominent in agrochemicals and serves as a key functional group in several commercial herbicides, including flumioxazin, thidiazimin, and trifludimoxazin. Therefore, we chose two molecular fragments to form a DHAD-targeted inhibitor scaffold (**I-6**). Molecular docking studies demonstrated that the inhibitors could stably bind within the DHAD active site, utilizing the α-hydroxycarboxylic acid fragment for metal ion coordination and the benzoxazinone skeleton for forming hydrophobic interactions with aromatic amino acids. The binding model of compound **I-6** with DHAD is similar to that of the substrate (Fig. 2a). This finding was validated by MST assays, which demonstrated the strong binding affinity (K_d = 2.79 μM) of **I-6** for DHAD in vitro. Moreover, 50 μg/mL **I-6** completely inhibited the germination of *A. thaliana* seeds (Fig. 2b). These findings not only confirm the viability of our rational design strategy but also provide a foundation for further studies on the interaction mechanisms between these inhibitors and DHAD.

Synthesis of the α-hydroxycarboxylic acid derivatives

A comprehensive synthesis scheme is depicted in Fig. 2c, with the detailed methods provided in Supplementary Note 1. The most challenging aspect of the synthesis route was determining a convenient and efficient method for the synthesis of α-hydroxycarboxylic acid fragments. Although several methods for C − H hydroxylation have been established[22–24], recent research has not yet fully realized green and environmentally benign synthetic approaches that avoid the use of expensive metal catalysts, hazardous stoichiometric oxidants, and reductants. In this study, we achieved α-C(sp^3)-H hydroxylation of carbonyls by employing cost-effective atmospheric oxygen (O_2) as an oxidant and cesium carbonate as a catalyst at ambient temperature.

According to previous studies, keto–enol tautomerism is among the core steps for the α-C(sp^3)-H hydroxylation of carbonyl groups[22,23]. Experiments conducted without the addition of alkali revealed no detectable products other than **I-4g** (Supplementary Table 2, entry 1). However, the introduction of various stoichiometries of inorganic alkali into the reaction mixture significantly enhanced the reaction efficiency. Notably, the use of Cs_2CO_3 as a base achieved impressive yields exceeding 95% (entries 2-5). A recent study by Li's group focused on the use of the organic base TBD for α-C − H hydroxylation[25]. However, in our experiments, organic bases such as TBD, DBU, *t*-BuOK, and Et_3N delivered yields of less than 70% (entries 6-9). In contrast, our results demonstrate that inorganic alkalies outperform their organic counterparts in catalyzing this specific reaction. Among all the inorganic bases tested, Cs_2CO_3 was the most effective and was considered the optimal reagent for achieving the α-C(sp^3)-H hydroxylation of carbonyl groups in high yields.

We subsequently explored the effects of varying stoichiometries of Cs_2CO_3 on the reaction (entries 10-13). When the quantity of Cs_2CO_3 exceeded 1.0 equivalents, the starting material **I-4g** was almost completely converted to the desired product **I-5g**. In contrast, the yield of **I-5g** significantly decreased in the presence of less than 1 equivalent of Cs_2CO_3. However, extending the reaction duration to 2 h or 3 h gave **I-5g** in excellent yield (greater than 90%) (entries 14-15). Additionally, we determined that light exposure had no significant effect on the reaction, as the yield remained consistent regardless of whether the reaction was conducted in the dark or light (entries 16 and 2). We then assessed the effect of the solvent on C − H hydroxylation (entries 17-24). Alternative solvents such as toluene, DMSO, DCM, THF, 1,4-dioxane, *n*-butanol, MeOH, and acetone were tested in lieu of DMF. However, none of these solvents outperformed DMF. Notably, alcohol

https://doi.org/10.1038/s41467-025-60489-8

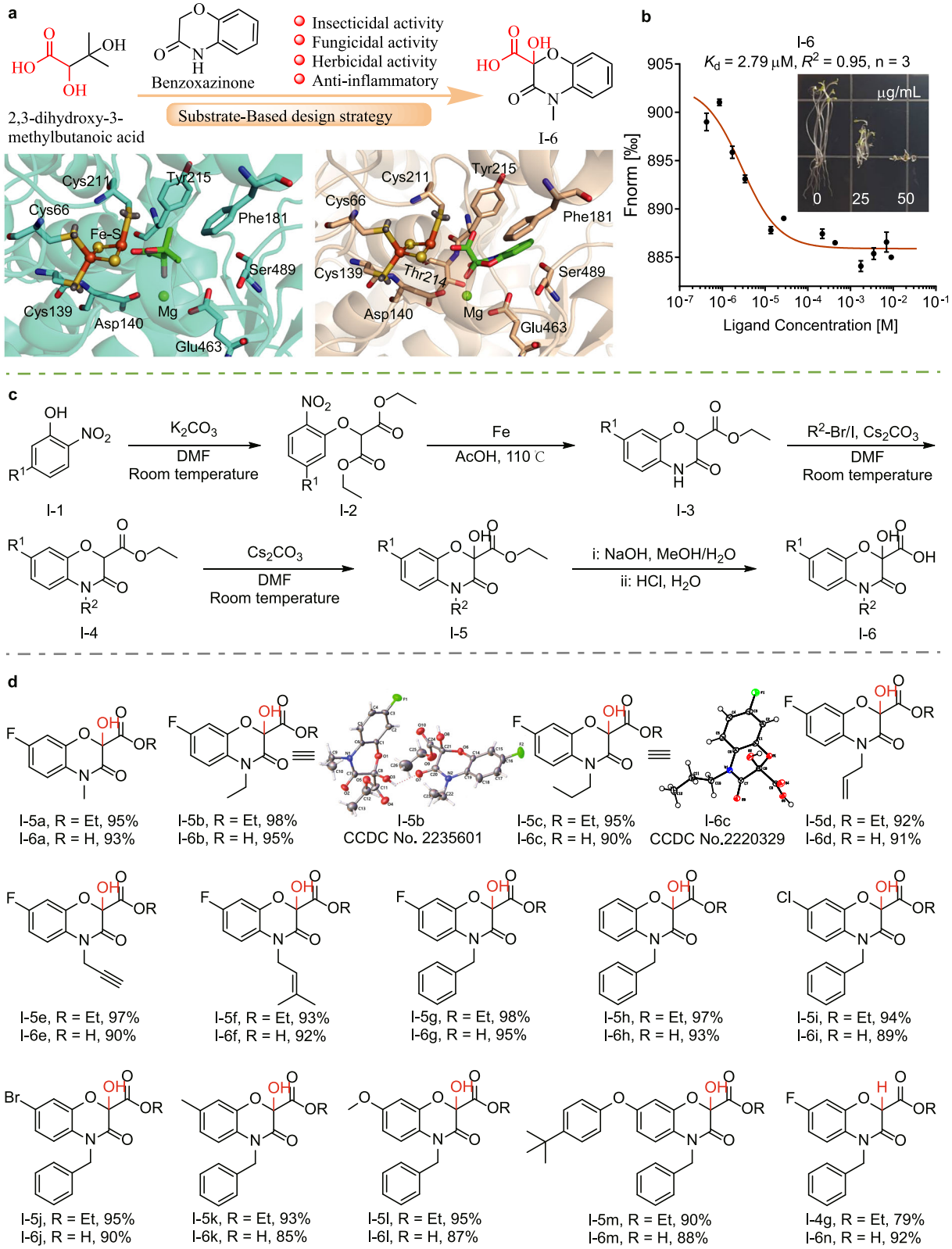

Fig. 2 | Design and synthesis of α-hydroxycarboxylic acid derivatives. a Design strategy for compounds **I-6** and the model of the substrate (2,3-dihydroxy-3-methylbutanoic acid) and **I-6** docked into *At*DHAD. Light blue indicates the substrate with *At*DHAD, and the light coffee color indicates **I-6** with *At*DHAD. **b** K_d value of compound **I-6** binding to *At*DHAD and the inhibitory effect of 25 and 50 μg/mL **I-6** on *A. thaliana* germination. The data are presented as the mean ± SD. **c** The general synthetic scheme for the title compounds. **d** Cs_2CO_3-initiated α-C (sp^3)-H hydroxylation of carbonyl derivatives **I-5a** – **I-5m** and target compounds **I-6a** – **I-6n**. The yields shown are for the isolated products. The crystal structures of compounds **I-5b** and **I-6c** are shown. Source data are provided as a Source Data file.

solvents, specifically *n*-butanol and MeOH, promoted the hydrolysis of ester groups under mildly alkaline conditions, which resulted in a higher conversion of **I-4g** but yielded only a minimal quantity of the target product **I-5g** (entries 22, 23). Furthermore, following the methodology of the Gnanaprakasam group[26], we attempted C − H hydroxylation using *t*-BuOK or TBD in DMSO (entries 25, 26), but these conditions produced only modest amounts of **I-5g** (yield < 30%). These experiments conclusively demonstrated that the synergistic combination of Cs_2CO_3 and DMF constituted the most favorable reaction conditions for the C(sp^3)-H hydroxylation of the benzoxazinone ring. We subsequently successfully converted the hydroxylated intermediates into the final compounds through ester bond hydrolysis. Moreover, we obtained single crystals of compounds **I-5b** and **I-6c** directly from the NMR solvent $CDCl_3$ that were suitable for characterization using single-crystal X-ray diffraction analysis. The detailed crystal structure data are provided in Supplementary Table 3 and 4. The structural characterization data for all the compounds are presented in Supplementary Note 1. The ^{1}H NMR and ^{13}C NMR spectra of compounds **I-5a** to **I-5m** and **I-6a** to **I-6n** are shown in Supplementary Fig. 2–55.

Possible mechanism of the C(sp^3)-H α-hydroxylation of benzoxazinone

To date, the reaction mechanism for C(sp^3)-H hydroxylation has not been conclusively determined. Under nitrogen, the reaction failed even after 24 h. Introducing radical inhibitors such as TEMPO or BHT did not affect the yield (Supplementary Fig. 56a). These results revealed that atmospheric oxygen is the oxygen source and that the reaction follows a nonradical pathway. Moreover, the NH-substituted compound **I-3a** did not react (Supplementary Fig. 56a), whereas the *N*-benzyl-substituted compound **I-4g** reacted normally. This discrepancy could be due to compound **I-3a** potentially forming two transition states, with one being incapable of C(sp^3)-H α-hydroxylation. After comparing the Gibbs free energy (ΔG) of the two transition states, ΔG_2 for the C = N transition state was found to be lower than ΔG_1 for the C = C transition state (14.02 kcal/mol vs. 19.11 kcal/mol), as calculated using the Gaussian 09 software (Supplementary Fig. 57). These results support the conclusion that the hydroxylation reaction is highly dependent on the keto-enol tautomerism of the C = C double bond rather than on the C = N double bond in the benzoxazinone ring.

The potential transition state was further elucidated through real-time NMR monitoring (Supplementary Fig. 56b). The C(sp^3)-H (H_a) signal (δ = 5.79 ppm) nearly vanished within 30 min, whereas the signals for H_b and H_c gradually diminished. Concurrently, the signals for H_b′ and H_c′ appeared and then weakened over time, disappearing completely after 60 min. Analysis of the changes in chemical shifts of the hydrogen proton signals over time revealed the initial occurrence of α-C(sp^3)-H carbonyl keto-enol tautomerism (**I-4g-1**), which subsequently leads to the generation of an intermediate that is stable in the reaction medium. The reaction mechanism of oxygen insertion into a C − H bond to form a C − O − O − H intermediate is widely recognized[23,25,27]. In our experiments, the chemical shifts of the other three hydrogen signals on the benzoxazinone ring shifted from 7.09 − 6.83 ppm to 6.68 − 6.41 ppm. This shift was attributed to the O − O − H group decreasing the charge density on the benzoxazinone ring, leading us to postulate that the intermediate structure is most likely **I-4g-2** (Supplementary Fig. 56b). Unfortunately, despite its apparent stability in the reaction system, this intermediate could not be isolated. Additionally, the introduction of a small quantity of trifluoroacetic acid (CF_3COOH, TFA) to the reaction system resulted in NMR spectra that matched those of the control compound **I-5g** with the addition of TFA. Therefore, the most plausible reaction mechanism is that under alkaline conditions, α-C (sp^3)-H carbonyl keto-enol tautomerism allows the generation of the reactive intermediate **I-4g-2** in the presence of atmospheric oxygen. Subsequent acid catalysis facilitates the cleavage of the peroxyl ether bond, leading to the formation of the final product **I-5g**.

Optimizing inhibitor activity on the basis of the target structure

Structure-based molecular optimization integrates detailed knowledge of the biological target into the drug design process, leading to more efficient and potentially more successful drug discovery and development[28]. The surface model of the compound **I-6**–DHAD structure (Supplementary Fig. 58) shows that the active pocket of *At*DHAD is a large internal cavity that is occupied by *N*-substituent groups and the benzoxazinone ring. These observations imply that the introduction of hydrophobic or bulky groups at these positions may increase the binding affinity of the inhibitor for DHAD (Supplementary Table 5). Furthermore, halogen bonding can be exploited for additional protein–ligand interactions[29]. Leveraging data from theoretical predictive models, we introduced a variety of substituents, such as halogens, hydrogen atoms, alkyl groups, alkoxypropargyl, and various substituted phenoxy groups, on either the benzene ring or at the *N*-position (Fig. 2d).

Inhibition of *A. thaliana* seed germination and revealing structure-activity relationship

We tested the inhibitory effects of all the compounds on *A. thaliana* seed germination (Supplementary Table 6). These compounds generally had a more pronounced inhibitory effect on root development than on hypocotyl growth. Notably, compound **I-6g**, with a *N*-benzyl substituent, inhibited both root and hypocotyl growth by more than 99%, outperforming the other *N*-substituted analogs (methyl, ethyl, and n-propyl) when tested at a concentration of 100 μg/mL. Among the compounds with unsaturated alkyl substituents, compound **I-6e** (propargyl) showed greater inhibitory activity than **I-6d** (allyl) and **I-6f** (isopentenyl) did, yet none were as effective as **I-6g** (benzyl). As a result, we maintained the benzyl group at the *N*-position and redirected our efforts to investigate how varying the substituent at the 7-position of the benzoxazinone nucleus affects inhibitory activity. Replacing the fluorine atom with other substituents, such as hydrogen (**I-6h**), chlorine (**I-6i**), bromine (**I-6j**), a methyl group (**I-6k**), and a methoxy group (**I-6l**), resulted in decreased inhibitory activity in comparison with that of compound **I-6g**. Compound **I-6m**, which contains a substituent at this position with large steric hindrance, demonstrated potent inhibition of root growth (-90%) but lower inhibition of hypocotyl growth at the same concentration.

Given the potent inhibitory effects of these compounds on *A. thaliana* seed germination, compounds **I-6c**, **I-6e**, **I-6g**, and **AA** were applied for postemergence treatment of two-week-old *A. thaliana* plants, which resulted in the cessation of new leaf production and the onset of leaf wilting (Fig. 3a). After 20 days of treatment with 200 μg/mL compound, the fresh weight inhibition by compound **I-6g** reached 76.01%, which was the highest among all the tested compounds and was significantly greater than that of **AA**, which exhibited 55.96% inhibition (Fig. 3b). Additionally, confocal laser scanning microscopy (CLSM) was used to observe the localization of DHAD in *Nicotiana benthamiana* leaves 24, 48, and 72 h after treatment with water or compound **I-6e**. The results revealed that DHAD was predominantly localized in chloroplasts (Supplementary Fig. 59). Our findings suggest that compounds with substantial steric bulk at the *N*-position are more effective DHAD inhibitors and that halogen F is a favorable substituent at the 7-position of the benzoxazinone ring. These experimental observations align well with our computational predictions.

Inhibition of DHAD by the α-hydroxycarboxylic acid derivatives

To investigate whether compound **I-6g** exerts its inhibitory effects on *A. thaliana* by specifically targeting the BCAA synthesis pathway, we conducted amino acid supplementation experiments. We

https://doi.org/10.1038/s41467-025-60489-8

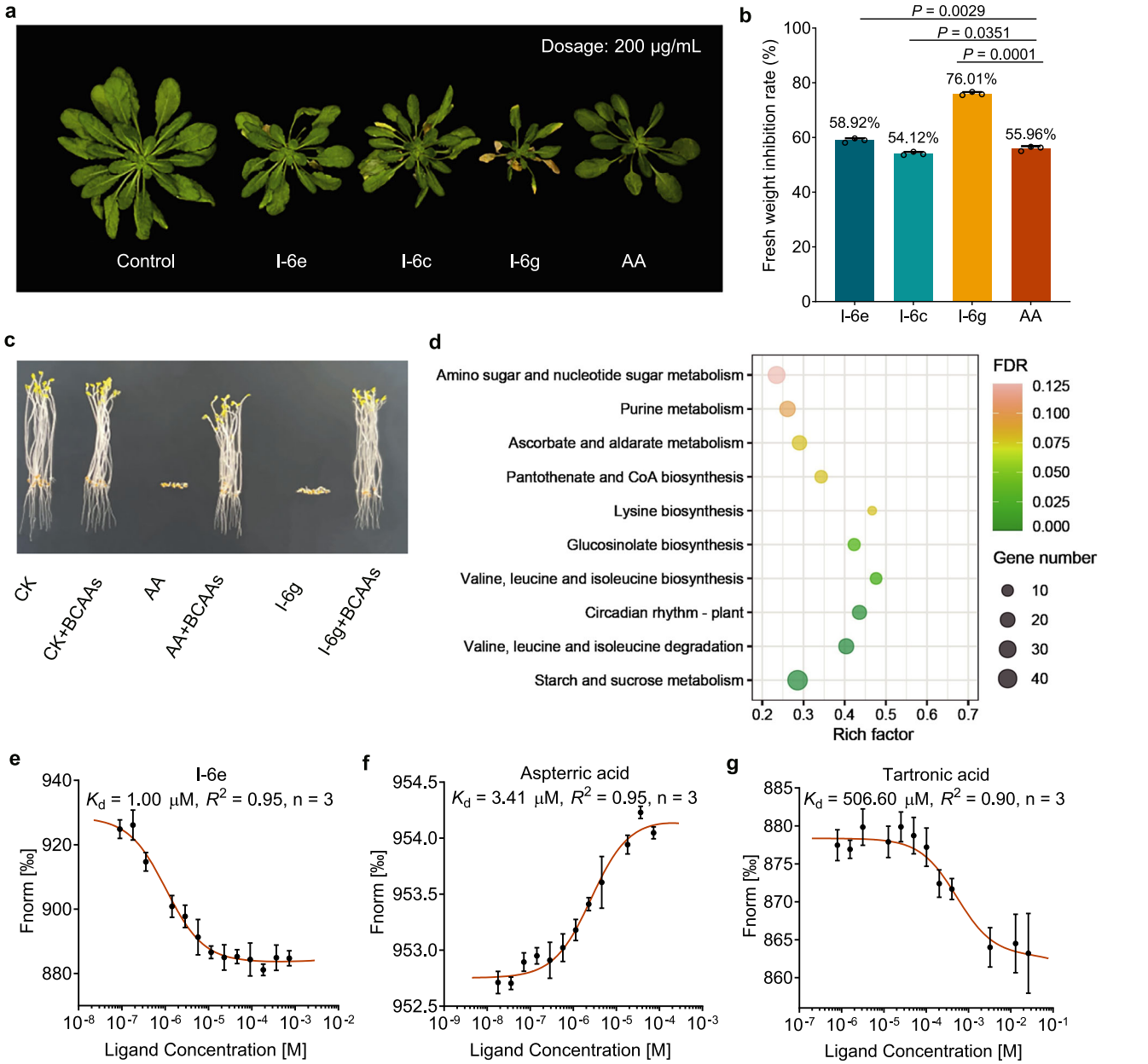

Fig. 3 | Effects of the α-hydroxylated acid derivatives on *Arabidopsis thaliana* growth and validation of targeting *At*DHAD. a Col-0 seedlings were grown in soil in pots and treated with **AA**, **I-6c**, **I-6e**, or **I-6g** at a dose of 200 μg/mL by foliar spray. **b** Fresh weight inhibition rates of *A. thaliana* plants 20 days after treatment with **AA**, **I-6c**, **I-6e**, or **I-6g**. The data are presented as the mean ± SD. One-way analysis of variance was used, and the data for the test compounds were compared with those of **AA**. Three independent replicates were performed. **c** Wild-type *A. thaliana* (Col-0) seedlings were grown on vertically oriented 1/2 MS media alone or media supplemented with 25 μg/mL BCAAs and treated with either 50 μg/mL **AA** or **I-6g**. Control seedlings were treated with 50 μg/mL DMSO. All the seedlings were grown under etiolation conditions for 7 days. **d** KEGG enrichment analysis of differentially expressed genes in the leaves of *A. thaliana* after treatment with **I-6g**. The vertical axis displays the pathway name, and the horizontal axis presents the Rich factor (sample number/background number). The greater the Rich factor is, the greater the degree of enrichment. Generally, the FDR ranges from 0–1, and the closer it is to zero, the more significant the enrichment. K_d values of **I-6e** (**e**), **AA** (**f**) and **TA** (**g**) binding to *At*DHAD. Each set of data comprises three replicates. R^2 is the correlation coefficient, and R^2 values closer to 1 represent a better fit. The data are presented as the mean ± SD. Source data are provided as a Source Data file.

attempted to grow *A. thaliana* Col-0 seeds on 1/2 MS media supplemented with 50 μg/mL **I-6g**, but germination was completely inhibited (Fig. 3c). Notably, the addition of 25 μg/mL BCAAs to the **I-6g**-supplemented medium restored germination and normal seedling development, with root and hypocotyl lengths similar to those observed in the DMSO-treated control (Supplementary Fig. 60a and 60b). The same effect was noted in the **AA**-treated positive control group, both on standard 1/2 MS medium and that with added BCAAs. These results implicate α-hydroxycarboxylic acid derivatives as inhibitors of BCAA biosynthesis.

We subsequently applied compound **I-6g** to *A. thaliana* plants via stem and leaf spraying for transcriptomic analysis. The results revealed that the top 10 pathways impacted by the treatment, as identified by KEGG database analysis, included both BCAA biosynthesis and degradation (Fig. 3d). As the duration of exposure to the compound increased, a broader spectrum of metabolic pathways was influenced, encompassing pathways such as photosynthesis–antenna proteins, starch and sucrose metabolism, and cysteine and methionine metabolism (Supplementary Fig. 60c). We further expressed and purified *At*DHAD proteins and measured the binding affinity (K_d value) of the

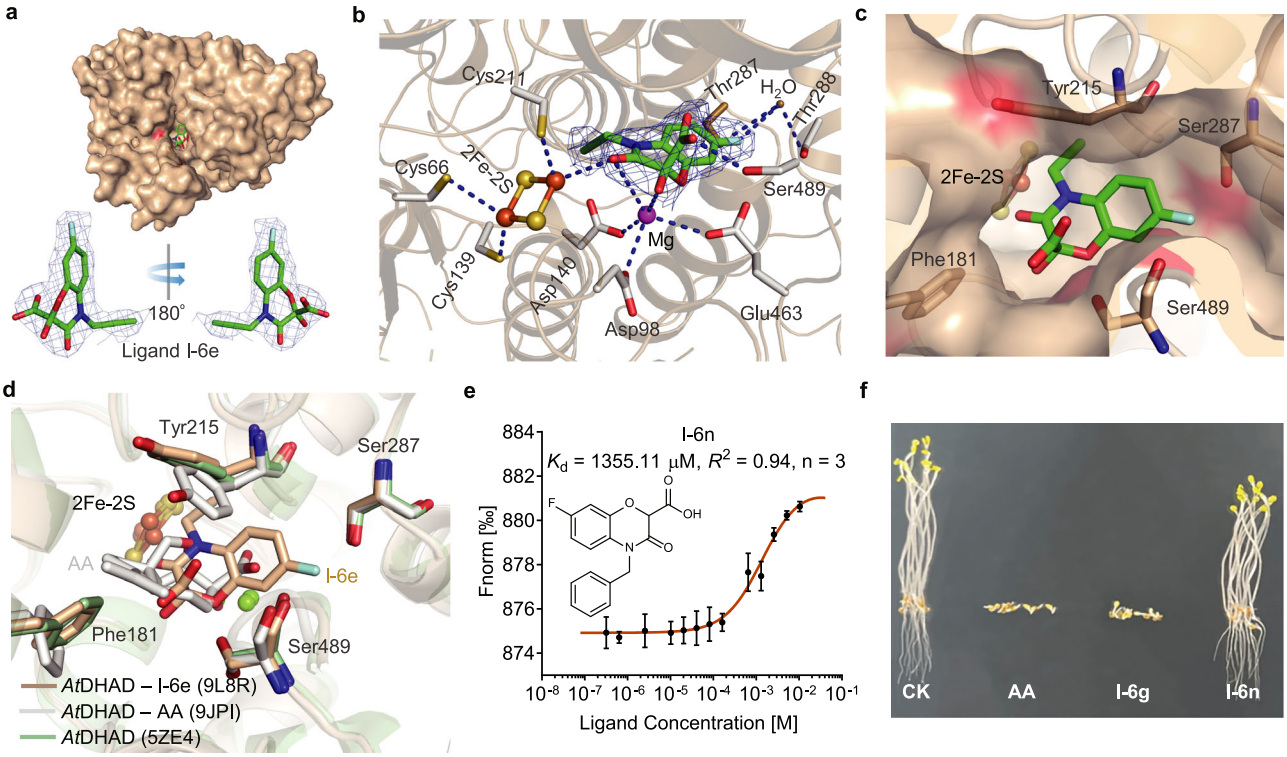

Fig. 4 | Mechanism of the interaction between I-6e and DHAD and the pharmacophore of the targeted DHAD inhibitor. a Cocrystal structure of *At*DHAD with **I-6e** and electron density contours (2Fo-Fc maps contoured at 1.0 σ) for the ligand in different orientations. **b** Interaction mode of compound **I-6e** in the active pocket of *At*DHAD (9L8R). The blue dashed lines represent hydrogen bonding interactions. **c** Surface model of the active pocket of the *At*DHAD–**I-6e** complex. The images were generated with PyMOL software. **d** Superimposition of the protein crystal structures of *At*DHAD with and without the inhibitor bound. **e** MST dose–response curve showing the interaction between **I-6n** and *At*DHAD. The data are presented as the mean ± SD. **f** Col-0 seedlings were grown on 1/2 MS medium and treated with **AA**, **I-6g**, or **I-6n** at a dose of 50 μg/mL. Source data are provided as a Source Data file.

agent for the protein using MST assays[30,31]. The MST data are shown in Fig. 3e, g. The K_d values for compounds **I-6c**, **I-6e**, **I-6g**, **I-6j**, and **I-6k** were all less than 3 μM, indicating their stronger affinities for the enzyme than that of the positive controls **TA** (K_d = 506.60 μM) and **AA** (K_d = 3.41 μM, Supplementary Table 7). These results support that α-hydroxycarboxylic acid derivatives target DHAD.

Cocrystal structure of AtDHAD-I-6e

Among all the compounds, **I-6e** exhibited the highest affinity for *At*DHAD, with a K_d value of 1.00 μM. Consequently, **I-6e** was selected as a ligand for cocrystallization with DHAD. The best crystals diffracted to a resolution of 2.19 Å (Supplementary Table 8). Despite the use of racemic compounds in our studies, only one enantiomer was observed to bind to DHAD.

The cocrystal structure of *At*DHAD with **I-6e** (Fig. 4a) reveals a clear electron density map that highlights the presence of ligand **I-6e** in the active pocket. The electron density contours (2Fo-Fc maps, contoured at 1.0 σ) for the ligand **I-6e** in different orientations are also shown in Fig. 4a. Additionally, the Fo-Fc omit map of **I-6e** (contoured at 1.0 σ) is presented in Supplementary Fig. 61. The [2Fe-2S] cluster, anchored at the base of the binding pocket, forms coordination bonds with three conserved cysteine residues, Cys211, Cys139, and Cys66. This leaves an open coordination site on one of the iron atoms, which is available to interact with ligand **I-6e**, aligning with previous studies[4,18,19]. Furthermore, Mg^{2+} ion in the pocket coordinates with three acidic residues, Asp98, Asp140, and Glu463, as well as with the hydroxyl group of **I-6e**, securing the small molecule in the active site. Notably, the carboxylic acid group of **I-6e** establishes a hydrogen bond with Ser489, and the fluorine atom interacts with the nearby residues Ser287 and Thr288 via a water-mediated hydrogen bond, further enhancing the binding stability of **I-6e** to DHAD (Fig. 4b, c).

Moreover, superimposing the three-dimensional DHAD structures (Fig. 4d) revealed distinct similarities in the binding interactions of **I-6e** and **AA** within the enzyme's active pocket. Notably, the π–π stacking interactions with Tyr215 and Phe181 were less prominent for **I-6e**. Correspondingly, the conformations of these aromatic residues remained akin to those observed in the absence of a bound inhibitor. Our comparative crystallographic analysis revealed additional interactions within the DHAD enzyme that are critical for inhibitor binding. These findings facilitate the design of a diverse array of inhibitor molecules with various structures that can specifically target DHAD.

α-hydroxycarboxylic acid is a crucial pharmacophore of targeted DHAD inhibitors

Analysis of the cocrystal structure of *At*DHAD with **I-6e** underscores the significant role of the α-hydroxycarboxylic acid moiety in enhancing the interaction between the inhibitor and its target. Thus, this raises the question of whether the hydroxyl group is essential for the efficacy of this series of DHAD inhibitors. Therefore, we synthesized a derivative, compound **I-6n**, which lacks this hydroxyl group. Subsequent in vitro binding assays revealed that **I-6n** displayed significantly reduced affinity, with a K_d of 1355.11 μM (Fig. 4e), which is nearly three orders of magnitude lower than that of **I-6g** (K_d = 1.43 μM). In line with these findings, the inhibitory effect of **I-6n** on seed germination was also markedly decreased compared with that of **I-6g**, even at a high concentration of 100 μg/mL (Fig. 4f). The combined in vitro and in vivo experimental results highlight the critical importance of the α-hydroxycarboxylic acid group for the activity of DHAD these inhibitors, confirming its status as a key pharmacophore.

Table 1 | Average fresh weight inhibition rates (%) after preemergence and postemergence treatment

No.	Preemergence treatment									Postemergence treatment		
	Rice	Wheat	Soya bean	Corn	*S. v.*	*A. t.*	*A. f.*	*A. a.*	*A. j.*	*E. c.*	*E. p.*	*A. r.*
I-6a	9.0	8.4	4.0	18.5	16.1	59.6	100.0	65.2	59.9	52.3	45.1	43.5
I-6b	22.3	0.8	30.5	5.0	32.3	13.3	100.0	43.5	44.1	49.1	46.0	42.3
I-6c	28.8	11.2	4.8	8.3	75.8	83.1	52.1	87.0	37.0	42.6	74.2	64.0
I-6d	3.5	6.5	8.2	22.0	50.0	88.6	37.0	8.7	55.5	41.4	50.4	57.7
I-6e	1.9	12.5	19.7	5.9	100.0	71.0	100.0	52.2	39.2	46.5	78.4	67.2
I-6f	7.9	11.9	15.8	6.6	87.1	78.0	42.0	78.3	64.3	41.6	49.9	30.6
I-6g	0.0	20.5	2.8	18.3	4.8	71.8	100.0	43.5	62.1	59.2	87.9	72.4
I-6h	4.6	18.5	7.3	12.1	75.8	12.5	100.0	100.0	67.4	26.3	49.6	44.8
I-6i	1.2	13.0	8.7	3.7	74.2	2.4	81.5	73.9	59.0	45.9	62.6	57.9
I-6j	5.1	7.5	0.3	21.5	66.1	20.8	100.0	87.0	76.7	42.3	64.7	54.0
I-6k	7.2	16.3	20.2	12.0	64.5	63.1	40.3	34.8	63.4	41.0	57.0	51.6
I-6l	13.0	3.3	9.3	20.0	30.6	53.7	100.0	78.3	48.0	47.2	66.4	56.4
I-6m	8.1	15.7	12.4	0.3	82.3	23.9	73.9	82.6	59.0	49.5	67.7	59.2
Penoxsulam	--	--	--	--	--	--	--	--	--	92.1	97.6	95.7

'-' not tested; '0' no inhibition; '100' complete inhibition; *S. v. Setaria viridis* P. Beauv., *A. t. Abutilon theophrasti* Medicus, *A. f. Avena fatua* L., *A. a. Alopecurus aequalis* Sobol., *A. j. Alopecurus japonicus* Steud., *E. c. Echinochloa crus-galli* P. Beauv., *E. p. Eclipta prostrata* L. and *A. r. Amaranthus retroflexus* L. Source data are provided as a Source Data file.

Using structure of I-6e to design targeted DHAD inhibitors

The glasshouse tests to examine the preemergence and postemergence herbicidal activities of compounds **I-6a** to **I-6m** provided important insights into their efficacy and selectivity. In these assays, water with 5% DMSO was used as a blank control, and penoxsulam, which targets AHAS, was used as a positive control. The ability of the synthetic compounds to inhibit weed or crop growth at a dose of 150 g ai/ha was evaluated. The results, as summarized in Table 1 and Supplementary Fig. 62, revealed that compounds **I-6c**, **I-6e**, **I-6g**, **I-6i**, **I-6j**, and **I-6m** inhibited the growth of the six weeds tested by more than 50%, as determined by weight. Notably, *Avena fatua* was the most effectively controlled by these compounds. In addition to their herbicidal activity, the safety of these compounds to crops was assessed upon preemergence treatment. Most of the compounds were safe for rice, with a fresh weight inhibition rate of less than 5%. Some compounds with certain crops, such as **I-6j** for soybean, **I-6m** for corn, and **I-6b** for wheat, had no significant harmful effects. Notably, compound **I-6e** demonstrated over 70% efficacy against broadleaf weeds such as *Abutilon theophrasti* Medicus and *Amaranthus retroflexus* and 100% efficacy against gramineous weeds such as *Setaria viridis* P. Beauv. and *A. fatua* and was less harmful to rice. Thus, compound **I-6e** is a particularly promising candidate as a lead structure for targeted DHAD inhibitors because of their potent herbicidal activity and crop safety.

Discussion

DHAD plays a critical role in the biosynthesis of BCAAs, which are essential for the growth and development of plants. This enzyme is responsible for dehydrating dihydroxy-acid substrates, yielding α-keto acids that serve as precursors of leucine, isoleucine, and valine. Although DHAD has been revealed to be a potential herbicidal target, no lead compounds with broad-spectrum herbicidal activity that target this enzyme have been identified[2,3]. Protein structure superposition revealed that the three cysteine residues involved in iron–sulfur coordination exhibit consistent conformations (Fig. 1c). However, the binding of the inhibitor to the active site induces a conformational shift in Phe181 and Tyr215, and the I177F mutation alters the stability of the binding of the inhibitor **AA** to DHAD. Also considering the binding model of the substrate to DHAD (Fig. 2a), coordination interactions with metal ions, hydrophobic interactions with Tyr215, Phe181, and Ile177, and hydrogen bonding interactions with Ser489 not only are crucial for the natural substrate's binding with DHAD but also constitute the fundamental forces enabling the inhibitor molecules to stably bind to the active site of DHAD.

Adopting a substrate-based molecular design approach, we utilized the α-hydroxycarboxylic acid moiety as a foundation unit and introduced an aromatic fragment to form hydrophobic interactions. The benzoxazinone ring is a prevalent scaffold in both medicinal chemistry and agrochemical design. Therefore, we combined the benzoxazinone moiety with α-hydroxycarboxylic acid units to design an inhibitor skeleton. Molecular docking simulations indicated that these derivatives can engage in coordination interactions with the 2Fe-2S cluster and Mg^{2+}, in addition to forming hydrophobic contacts with Phe181 and hydrogen bonding interactions with Ser489. Our design strategy offers a different and effective approach for developing more potent and selective herbicidal compounds that target different sites of action.

Furthermore, by utilizing cost-effective atmospheric oxygen (O_2) as an oxidant and cesium carbonate as a catalyst at ambient temperature, we developed an efficient and eco-friendly method for synthesizing α-hydroxycarboxylic acids without the need for expensive metal catalysts. In contrast to previous studies[25,26,32], we discovered that an inorganic base (Cs_2CO_3) outperforms an organic base in our reaction and demonstrates compatibility with a broad spectrum of substrates. Unfortunately, this method does not allow control of the chirality of the compound. Additionally, during chiral resolution, the compound underwent spontaneous racemization in the solvent. This phenomenon was attributed to the formation of hydrogen bonds[33,34], as supported by the detection of such bonds in the crystal structure of compound **I-5b** (Fig. 2c). As a result, the synthesized target compounds, which were employed for bioactivity evaluations, are racemic mixtures.

Furthermore, our research revealed that α-hydroxycarboxylic acid derivatives act as inhibitors of the BCAA synthesis pathway by targeting DHAD. BCAA deficiency leads to distinct phenotypes in plants, including stunted growth, underdeveloped root systems, and reduced root lengths[9]. In our study, treatment with these derivatives or **AA** induced identical phenotypic symptoms, which were reversed upon supplementation of BCAAs in the medium (Fig. 3c). Transcriptomic analysis further highlighted significant changes in BCAA biosynthesis and metabolism at both 24 h (Fig. 3d) and 72 h (Supplementary Fig. 60c), confirming the influence of hydroxycarboxylic acid derivatives on BCAA production. The in vitro assays revealed that the K_d value of **I-6e** with DHAD was 1.00 μM, indicating its stronger affinity

for DHAD than that of dihydroxyisovalerate (K_d = 5.39 μM). Additionally, we successfully determined the crystal structure of the *At*DHAD–**I-6e** complex at a resolution of 2.19 Å and observed that the binding patterns of **I-6e** and **AA** within the active pocket were markedly different. In addition to the coordination interaction, the presence of hydrogen bonds between the inhibitor and Ser489, as well as the interactions of the halogen atom of the inhibitor with Thr288 through a water-mediated hydrogen bond (Fig. 4b), contributed to the superior binding stability of **I-6e** to DHAD compared with that of **AA**. The **I-6e** binding site of DHAD paves the way for the design of structurally diverse targeted DHAD inhibitors. Furthermore, our findings suggest that the α-hydroxycarboxylic acid functional group is crucial for enhancing inhibitor binding stability and retaining in vitro herbicidal activity, indicating that it is an essential pharmacophore of targeted DHAD inhibitors. Notably, compound **I-6e** displayed a broad spectrum of herbicidal effects, most notably completely inhibiting the growth of *S. viridis* and *A. fatua* while causing little harm to rice at a dosage of 150 g ai/ha (Table 1).

In summary, we present a class of inhibitor molecules that target DHAD designed via a substrate-based design strategy. Within this class, **I-6e** has emerged as a particularly promising DHAD inhibitor because of its potent herbicidal efficacy and favorable safety profile in crops. Crystallographic analysis revealed that the binding pattern of **I-6e** with DHAD is distinct from that of the **AA**-DHAD interaction, highlighting a different site of action that can be exploited when designing inhibitory molecules. This discovery opens potential pathways for the development of more selective and efficient DHAD-targeted herbicides and provides a theoretical foundation for the development of targeted DHAD inhibitors, which hold great promise for agricultural applications.

Methods

Chemical synthesis and analysis

Reagents were purchased from Energy Chemical, Aladdin, JK Chemical, Macklin and other commercial suppliers. **AA** was purchased from GlpBio Technology. Biological reagents and consumables were purchased from Vazyme, Yeasen and other commercial suppliers. Primer synthesis was conducted by GenScript Biotechnology (Nanjing, China). Reactions were monitored by thin layer chromatography (TLC) on silica. Silica gel (200–300 mesh) for column chromatography was purchased from Qingdao Marine Chemical Inc., China. ^{1}H NMR and ^{13}C NMR spectra were collected with a JNM-ECZ500R instrument (500 MHz, JEOL, Japan) in $CDCl_3$ or DMSO-d_6 and with tetramethylsilane (TMS) as the internal standard. The NMR data were analyzed using MestReNova 14.0.0 software. High-resolution electrospray ionization mass spectrometry (HR-ESI–MS) data were obtained with an Agilent 6210 TOF LC–MS spectrometer (Agilent, USA). High-performance liquid chromatography (HPLC) was conducted using an Eclipse XDB-C18 column (5 μm, 4.6 × 250 mm; AkzoNobel, China) on an Agilent 1260 liquid chromatograph (Agilent Technologies, USA). HPLC gradient elution was performed with a linear gradient of 60–95% MeOH–H_2O over 15 min followed by 95% MeOH for 3 min and then 60% MeOH–H_2O for 3 min; the flow rate was 1 mL/min. Compound X-ray single-crystal diffraction data were collected on a SMART APEX DUO CCD area detector diffractometer (Bruker AXS, Madison, WI) using Mo or Ga Kα radiation at 100 (2) K. The diffraction profiles were integrated, and structural analysis was performed using SAINT Plus software (Bruker AXS, Madison, WI) and the SHELXS97 program (University of Gottingen, Gottingen, Germany), respectively. The detailed crystal structure data are provided in Supplementary Table 3 and 4.

Real-time NMR monitoring

Real-time NMR was performed to monitor reaction process[35,36]. Because the monitored reaction proceeds slower in DMSO than in DMF, DMSO-d_6 was used as the solvent instead of DMF-d_7, and an excess of Cs_2CO_3 (1.5 eq) was added to ensure that the reaction proceeded completely. Compound **I-4g** (50 mg, 0.15 mmol) was dissolved in 3 mL of DMSO-d_6, and the time after the addition of Cs_2CO_3 (0.225 mmol) and stirring at room temperature was measured. The mixture (volume of 600 μL) was quickly transferred to an NMR tube after 10 min, 20 min, 30 min, and 60 min, and NMR data were collected. The last sample (60 min) was analyzed again after the addition of TFA (30 μL) to the tube. As a control, compound **I-5g** (10 mg, 0.03 mmol) was mixed with 600 μL of DMSO-d_6 and 0.045 mmol of Cs_2CO_3 and stirred at room temperature for 60 min. Then, 30 μL of TFA was added to the reaction mixture, and NMR data were collected. All NMR data were collected at 25 °C and analyzed using MestReNova 14.0.0 software.

Molecular docking

The crystal structure of *At*DHAD (PDB ID: 5ZE4) was downloaded from the RCSB Protein Data Bank. The 3D structures of our compounds were prepared using SYBYL-X 2.0. The [2Fe-2S] cluster was chosen as the center of the binding pocket. The energies of the ligand and receptor were optimized on the SYBYL platform, and the other parameters were set to the defaults according to the Sybyl user guide. A total of 200 runs were performed, after which we selected the top-ranked conformation as the most suitable binding conformation. The total score was used as a reference for binding strength comparison[37,38].

Plant materials and growth conditions

Wild-type *A. thaliana* Col-0 seeds were provided by L R. Wei. *N. benthamiana* seeds were provided by M F. Feng. *A. thaliana* seeds were incubated at 4 °C for 3 days before sowing. Afterward, *A. thaliana* was germinated in the cultivation substrate, transplanted into a small pot, and grown in a light incubator with a light/dark cycle of 8 h (22 °C)/16 h (22 °C) for 3–4 weeks. *N. benthamiana* plants were grown in a growth chamber with a light/dark cycle of 16 h (25 °C)/8 h (25 °C). Weed and crop seeds were planted in soil and grown in a glasshouse under natural conditions at temperatures ranging from 20 °C to 32 °C.

Germination of *A. thaliana* seeds

A. thaliana seeds (Col-0) were surface sterilized with chlorine gas for 3 h and vernalized at 4 °C for 3 days before use. Afterward, the *A. thaliana* seeds were sown in Petri dishes (10 cm × 10 cm) containing 1/2 MS media (2.2 g/L MS salts, 10.0 g/L sucrose, and 8 g/L agar) supplemented with different concentrations of various agents (compounds **I-6** to **I-6n** or **AA** at 3.13 μg/mL, 6.25 μg/mL, 12.5 μg/mL, 25 μg/mL, 50 μg/mL, or 100 μg/mL). Separately, BCAAs (m_{Leu}:m_{Ile}:m_{Val} = 1:1:1, total final concentration of 25 μg/mL) was added to 1/2 MS medium. ~12–15 surface-sterilized Col-0 seeds were sown on the 1/2 MS medium and cultivated at 22 °C in the dark for 7 days. Then, ten germinated seeds were randomly selected from each Petri dish, and the lengths of the hypocotyls and roots were measured. The root or hypocotyl inhibition rate was calculated as equation 1:

$$\begin{aligned}\text{Inhibition rate} = &(\text{Length in control group}\\ &-\text{Length in treatment group})\\ &/\text{Length in control group} * 100\end{aligned} \quad (1)$$

All the experiments were independently repeated three times.

Postemergence treatment of *A. thaliana*

Compounds **I-6e**, **I-6c**, **I-6g**, and **AA** were dissolved in DMSO and diluted with 0.5% aqueous Tween 80 to a final concentration of 200 μg/mL, with a final concentration of DMSO of less than 5%. The prepared solutions (1 mL) were sprayed evenly on the stems and leaves of 2-week-old *A. thaliana* plants exhibiting good growth, and the plants were grown in a light incubator for 20 days.

Protein expression, purification, and cocrystal structure determination

The plasmid *At*DHAD-pET was transformed into *E. coli* BL21 (DE3). After IPTG induction of protein expression, the bacterial precipitate was collected by ultracentrifugation. Next, lysozyme and benzonase nuclease were added and crushed using an ultrasonic crusher. After ultracentrifugation, the supernatant was collected and separated by purification using Ni-NTA affinity column in a Vigor anaerobic chamber. During *E. coli* BL21 (DE3) culture, $FeCl_3$ and L-Ara were added to stabilize the [2Fe-2S] cluster in the protein. We obtained a high-purity *At*DHAD protein by optimizing the expression and purification conditions. We obtained a high-purity *At*DHAD protein by optimizing the expression and purification conditions[2]. The protein was diluted with Buffer C (150 mM NaCl, 25 mM Tris-HCl, pH 8.0) to a final protein concentration of 10 mg/mL. The mixed solution of protein and **I-6e** was incubated on ice for 1–2 h in an anaerobic box, and then crystallization was carried out by the sitting-drop vapor diffusion method at 16 °C. Diffraction of the tetragonal orange cocrystals was performed in 1.0 M ammonium sulfate and 0.1 M ammonium acetate (pH 5.24) in the absence of oxygen. All the crystals were flash-cooled in liquid nitrogen after being cryoprotected with glycerol. The data were collected at 100 K at Beam Line 19U1 in the Shanghai Synchrotron Radiation Facility (SSRF). All datasets were indexed, integrated, and scaled using the HKL3000 package[39]. Finally, the crystal structure data (Supplementary Table 8) were obtained with an R-free value of 0.2311, R-work value of 0.1814 and resolution of 2.19 Å.

MST assay

With purified *At*DHAD in hand, buffer replacement and lysine residue labeling of the *At*DHAD protein in solution (10 μM) were performed according to standard operating procedures using the Protein Labeling Kit RED-NHS 2nd Generation (MO-L011, NanoTemper). Ligand solutions at various concentrations (ranging from 10^{-10} M to 10^{-1} M) were incubated with 50 nM dye-labeled tagged protein at 4 °C for 30 min in assay buffer (3.2 mM Na_2HPO_4, 0.5 mM KH_2PO_4, 1.3 mM KCl, 135 mM NaCl, 0.05% Tween 20, pH 7.4). The samples were subsequently loaded into label-free standard capillaries (MO-K022, NanoTemper) for data collection on a Monolith NT.115 (MO. Control). The excitation power was 100% or 40%, and the MST power was medium. The MST data were analyzed by MO.Affinity Analysis, and GraphPad Prism 7.00 were used for plot construction.

Determination of subcellular localization via CLSM

The full-length coding sequence of *At*DHAD was cloned and inserted into the p2300-YFP vector to generate the p2300-YFP-*At*DHAD construct. The constructed plasmid p2300-YFP-*At*DHAD was subsequently transformed into *Agrobacterium tumefaciens* strain GV3101 cells. After incubation in YEB liquid medium at 200 × *g* for 3 h, the bacteria were collected by centrifugation at 4000 × *g* for 4 min, and after discarding the supernatant, the cells were resuspended in infiltration buffer (10 mM MES, 10 mM $MgCl_2$, pH 5.6, and 100 μM acetosyringone) to an OD_{600} of 0.6. Fully expanded leaves of *N. benthamiana* plants at the 6–7-leaf stage were infiltrated with *Agrobacterium* cultures using 1 mL needleless syringes and grown in a growth chamber at 25 °C with a 16 h light/8 h dark photoperiod. After 2 days of low-light culture, the plants were observed by confocal microscopy. Confocal images were captured with an inverted Zeiss LSM 900 Airyscan 2 and a 20× water immersion objective lenses. YFP was excited at a wavelength of 488 nm, and emission in the range of 497–520 nm was captured. To visualize chloroplasts, chlorophylls were excited at a wavelength of 488 nm, and emission in the range of 660–720 nm was captured. Images were processed using a Zeiss LSM 900 Airyscan 2. Signal overlap was observed by merging the YFP-*At*DHAD and chlorophyll fluorescence signals.

Transcriptomic analysis

The stems and leaves of *A. thaliana* plants were sprayed with compound **I-6g**, and samples without roots were collected 24 h and 72 h later and frozen with liquid nitrogen. Then, RNA extraction and data analysis were performed according to standard methods (Shanghai Personalbio Technology Co., Ltd., China). DESeq was used to analyze differential gene expressions, and genes were considered differentially expressed when they met the criteria of $|\log_2\text{FoldChange}|$ å 1 and P value < 0.05. KEGG enrichment analysis (KAAS, bidirectional best hit) of the differentially expressed genes considered the enrichment degree determined by the Rich factor, the false discovery rate (FDR) and the number of genes enriched in each pathway. The Rich factor is the ratio of the number of differentially enriched genes and the number of annotated genes in a pathway. The greater the rich factor is, the greater the degree of enrichment. Generally, FDR ranges from 0-1. The closer the value is to zero, the more significant the enrichment. The top 10 KEGG pathways with the smallest FDR values (the pathways enriched in the greatest number of differentially expressed genes), were selected for display (http://www.kegg.jp/). Three replicates were used in the experiment. The raw transcriptome data were uploaded to the NCBI database (PRJNA1229804).

Preemergence herbicidal activity

Weed and crop seeds with an emergence rate greater than 95% were evenly planted in small pots, provided sufficient water, and allowed to grow in a glass greenhouse for 12 h. Then, solutions of the test compounds were evenly sprayed on the surface of the soil at a dose of 150 g ai/ha. Each treatment contained three replicates. After 21 days, the weeds above the soil surface were removed, and the fresh weight was measured with a balance with a precision of 1/10,000 (BSA2245, BSISL). All experiments were independently repeated three times. The average fresh weight inhibition rates were calculated as eq. 2 and presented in Table 1.

$$\text{Fresh weight inhibition rate} = (\text{Weight in control group} - \text{Weight in treatment group}) / \text{Weight in control group} * 100 \quad (2)$$

Postemergence herbicidal activity

Weeds and crops were grown to the 2–3-leaf stage in a greenhouse, with 10 plants in each pot. The test compound solutions were sprayed on the plants with a WPSH-500D bioassay spray tower (Nanjing Institute of Agricultural Mechanization) at a dose of 150 g ai/ha. The instrument was operated with a disk diameter of 50 cm, a nozzle aperture of 0.3 mm, a spray pressure of 0.3 MPa, a dropper diameter of 100 μm, and a nozzle flow rate of 90 mL/min. Each treatment consisted of three replicates. After 21 days of treatment, 10 weeds above the soil surface were removed, the fresh weight was measured, and the fresh weight inhibition rate was calculated. The average values obtained for the fresh weight inhibition rates are shown in Table 1.

Mapping and data processing

All the data were summarized in Microsoft Excel 2016. Histogram analysis and two-way analysis of variance were performed with GraphPad Prism 7.00. Image processing was performed with Adobe Photoshop 2021. The structures of the compounds were constructed with ChemBioDraw 14.0.

Reporting summary

Further information on research design is available in the Nature Portfolio Reporting Summary linked to this article.

Data availability

The protein crystallographic data have been deposited in the Protein Data Bank with accession code 9L8R. The RNA-seq data are available in

the National Center for Biotechnology Information SRA database under accession PRJNA1229804. The crystallographic data have been submitted to the Cambridge Crystallographic Data Center under ID 2235601 and 2220329. Source data are provided with this paper.

References

1. Guo, S. X., He, F., Song, B. A. & Wu, J. Future direction of agrochemical development for plant disease in China. *Food Energy Secur* **10**, e193 (2021).
2. Yan, Y. et al. Resistance-gene-directed discovery of a natural-product herbicide with a new mode of action. *Nature* **559**, 415–418 (2018).
3. Zhang, P. et al. Cyanobacterial dihydroxyacid dehydratases are a promising growth inhibition target. *ACS Chem. Biol.* **15**, 2281–2288 (2020).
4. Amorim Franco, T. M. & Blanchard, J. S. Bacterial branched-chain amino acid biosynthesis: structures, mechanisms, and drugability. *Biochemistry* **56**, 5849–5865 (2017).
5. Lonhienne, T. et al. Structures of fungal and plant acetohydroxyacid synthases. *Nature* **586**, 317–321 (2020).
6. Liang, Y. F. et al. The chemical mechanisms of the enzymes in the branched-chain amino acids biosynthetic pathway and their applications. *Biochimie* **184**, 72–87 (2021).
7. Bayaraa, T. et al. Dihydroxy-acid dehydratases from pathogenic bacteria: emerging drug targets to combat antibiotic resistance. *Chemistry* **28**, e202200927 (2022).
8. Lonhienne, T. et al. Structural basis of resistance to herbicides that target acetohydroxyacid synthase. *Nat. Commun.* **13**, 3368–3378 (2022).
9. Zhang, C. et al. Dihydroxyacid dehydratase is important for gametophyte development and disruption causes increased susceptibility to salinity stress in Arabidopsis. *J. Exp. Bot.* **66**, 879–888 (2015).
10. Flint, D. H. & Nudelman, A. Studies on the active site of dihydroxy-acid dehydratase. *Bioorg. Chem.* **21**, 367–385 (1993).
11. Zang, X. et al. Structural bases of dihydroxy acid dehydratase inhibition and biodesign for self-resistance. *BioDesign Res* **6**, 0046 (2024).
12. Horne, R. I. et al. Discovery of potent inhibitors of alpha-synuclein aggregation using structure-based iterative learning. *Nat. Chem. Biol.* **20**, 634–645 (2024).
13. Li Petri, G., Di Martino, S. & De Rosa, M. Peptidomimetics: an overview of recent medicinal chemistry efforts toward the discovery of novel small molecule inhibitors. *J. Med. Chem.* **65**, 7438–7475 (2022).
14. Wang, L. et al. Therapeutic peptides: current applications and future directions. *Signal Transduct. Target Ther.* **7**, 48 (2022).
15. Sadybekov, A. A. et al. Synthon-based ligand discovery in virtual libraries of over 11 billion compounds. *Nature* **601**, 452–459 (2021).
16. Sadybekov, A. V. & Katritch, V. Computational approaches streamlining drug discovery. *Nature* **616**, 673–685 (2023).
17. Flint, D. H., Emptage, M. H., Finnegan, M. G., Fu, W. & Johnson, M. K. The role and properties of the iron-sulfur cluster in Escherichia coli dihydroxy-acid dehydratase. *J. Biol. Chem.* **268**, 14732–14742 (1993).
18. Flint, D. H. & Emptage, M. H. Dihydroxy acid dehydratase from spinach contains a [2Fe-2S] cluster. *J. Biol. Chem.* **263**, 3558–3564 (1988).
19. Bashiri, G. et al. The active site of the Mycobacterium tuberculosis branched-chain amino acid biosynthesis enzyme dihydroxyacid dehydratase contains a 2Fe-2S cluster. *J. Biol. Chem.* **294**, 13158–13170 (2019).
20. Zamani, L. et al. Docking, synthesis, antifungal and cytotoxic activities of some novel substituted 4H-benzoxazin-3-one. *Polycycl. Aromat. Compd.* **41**, 347–367 (2019).
21. Nagaraju, A., Kumar Nukala, S., Narasimha Swamy Thirukovela, T. & Manchal, R. In vitro anticancer and in silico studies of some 1,4-benzoxazine-1,2,4-oxadiazole hybrids. *ChemistrySelect* **6**, 3318–3321 (2021).
22. Sim, S.-B. D., Wang, M. & Zhao, Y. Phase-transfer-catalyzed enantioselective α-hydroxylation of acyclic and cyclic ketones with oxygen. *ACS Catal.* **5**, 3609–3612 (2015).
23. Liang, Y. F. & Jiao, N. Highly efficient C-H hydroxylation of carbonyl compounds with oxygen under mild conditions. *Angew. Chem. Int. Ed.* **53**, 548–552 (2014).
24. Chuang, G. J., Wang, W., Lee, E. & Ritter, T. A dinuclear palladium catalyst for alpha-hydroxylation of carbonyls with O_2. *J. Am. Chem. Soc.* **133**, 1760–1762 (2011).
25. Wang, Y., Lu, R., Yao, J. & Li, H. 1,5,7-Triazabicyclo[4.4.0]dec-5-ene enhances activity of peroxide intermediates in phosphine-free alpha-hydroxylation of ketones. *Angew. Chem. Int. Ed.* **60**, 6631–6638 (2021).
26. Chaudhari, M. B., Sutar, Y., Malpathak, S., Hazra, A. & Gnanaprakasam, B. Transition-metal-free C-H hydroxylation of carbonyl compounds. *Org. Lett.* **19**, 3628–3631 (2017).
27. Sterckx, H., Morel, B. & Maes, B. U. W. Recent advances in catalytic aerobic oxidation of C(sp^3)-H bonds. *Angew. Chem. Int. Ed.* **58**, 7946–7970 (2019).
28. Liu, R., Li, X. & Lam, K. S. Combinatorial chemistry in drug discovery. *Curr. Opin. Chem. Biol.* **38**, 117–126 (2017).
29. Metrangolo, P. & Resnati, G. Chemistry. halogen versus hydrogen. *Science* **321**, 918–919 (2008).
30. Huang, L. & Zhang, C. Microscale thermophoresis (MST) to detect the interaction between purified protein and small molecule. *Methods Mol. Biol.* **2213**, 187–193 (2021).
31. Parker, J. L. & Newstead, S. Molecular basis of nitrate uptake by the plant nitrate transporter NRT1.1. *Nature* **507**, 68–72 (2014).
32. Yu, S.-M., Cui, K., Lv, F., Yang, Z.-Y. & Yao, Z.-J. Aerobic α-hydroxylation of β-keto esters and amides by co-catalysis of SmI3 and I2 under mild base-free conditions. *Tetrahedron Lett.* **57**, 2818–2821 (2016).
33. Ikuma, N. et al. Spontaneous racemization and epimerization behavior in solution of chiral nitroxides. *Org. Lett.* **7**, 1797–1800 (2005).
34. Wu, H. & West, A. R. Thermally-induced homogeneous racemization, polymorphism, and crystallization of pyroglutamic acid. *Cryst. Growth Des.* **11**, 3366–3374 (2011).
35. Jaroszewicz, M. J. et al. Time- and site-resolved kinetic NMR for real-time monitoring of off-equilibrium reactions by 2D spectrotemporal correlations. *Nat. Commun.* **13**, 833 (2022).
36. Smith, M. J. et al. Real-time NMR monitoring of biological activities in complex physiological environments. *Curr. Opin. Struct. Biol.* **32**, 39–47 (2015).
37. He, B. et al. Design and syntheses of proherbicides targeting 4-hydroxyphenylpyruvate dioxygenase. *J. Agric. Food Chem.* **73**, 4507–4517 (2025).
38. He, B. et al. Development and biological evaluation of new diphenyl ether formylhydrazide compounds as potent inhibitors of succinate dehydrogenase. *J. Agric. Food Chem.* **72**, 26133–26141 (2024).
39. Otwinowski, Z. & Minor, W. Processing of X-ray diffraction data collected in oscillation mode. *Methods Enzymol.* **276**, 307–326 (1997).

Acknowledgements

We thank the staff at beamline BL17U1 of the Shanghai Synchrotron Radiation Facility for assistance with data collection. This work was supported by the National Key Research and Development Program of China (2021YFD1700100 to B.H.), the National Natural Science Foundation of China (32202356 to B.H., 32472625 to Y.Y.) and the Natural Science Foundation of Jiangsu Province (BK20221002 to B.H.).

Author contributions

Y.Y. and J.Z. conceived and designed the project; B.H. and Y.H. performed the molecular computational simulations, compound synthesis, bioactivity assays and data analysis; D.L. and X.Z. purified the protein and determined the crystal structure; X.H. and W.C. performed the in vitro activity tests; J.Y. performed the bioinformatics analysis; M.F., P.C., L.W., Y.L., W.Y., J.L. and Z.F. conducted the plant growth and the herbicidal activity experiments; and B.H. and Y.H. wrote the manuscript with contributions from all the authors. All the authors read and discussed the manuscript.

Competing interests

The authors declare no competing interests.

Additional information

Supplementary information The online version contains supplementary material available at https://doi.org/10.1038/s41467-025-60489-8.

Correspondence and requests for materials should be addressed to Jiahai Zhou or Yonghao Ye.

Peer review information *Nature Communications* thanks the anonymous reviewers for their contribution to the peer review of this work. A peer review file is available.